Progress in PHOTOVOLTAICS

PROGRESS IN PHOTOVOLTAICS: RESEARCH AND APPLICATIONS
Prog. Photovolt: Res. Appl. 2014; **22**:300–307
Published online 2 August 2012 in Wiley Online Library (wileyonlinelibrary.com). DOI: 10.1002/pip.2259

RESEARCH ARTICLE

Towards high-efficiency multi-junction solar cells with biologically inspired nanosurfaces

Peichen Yu[1]*, Meng-Yih Chiu[1], Chia-Hua Chang[1], Chung-Yu Hong[1,2], Yu-Lin Tsai[1], Hau-Vei Han[1] and Yu-Rue Wu[2]

[1] Department of Photonics, Institute of Electro-Optical Engineering, National Chiao Tung University, 1001 University Road, Hsinchu, 300 Taiwan
[2] Arima Photovoltaic & Optical Corporation, No. 349, Sec. 2, Renhe Road, Dasi, Taoyuan 33547, Taiwan

ABSTRACT

Multi-junction solar cells offer extremely high power conversion efficiency with minimal semiconductor material usage, and hence are promising for large-scale electricity generation. However, suppressing optical reflection in the UV regime is particularly challenging due to the lack of adequate dielectric materials. In this work, bio-inspired antireflective structures are demonstrated on a monolithically grown $Ga_{0.5}In_{0.5}P/In_{0.01}Ga_{0.99}As/Ge$ triple-junction solar cell, which overcome the limited optical response of reference devices. The fabricated device also exhibits omni-directional enhancement of photocurrent and power conversion efficiency, offering a viable solution to concentrated illumination with large angles of incidence. A comprehensive design scheme is further developed to tailor the reflectance spectrum for maximum photocurrent output of tandem cells. Copyright © 2012 John Wiley & Sons, Ltd.

Supporting information may be found in the online version of this article.

KEYWORDS

biomimetic nanostructures; sub-wavelength structures; solar cells; photovoltaic

***Correspondence**

Peichen Yu, Department of Photonics, Institute of Electro-Optical Engineering, National Chiao Tung University, 1001 University Road, Hsinchu, 300 Taiwan.
E-mail: yup@faculty.nctu.edu.tw

Received 10 October 2011; Revised 21 December 2011; Accepted 21 May 2012

1. INTRODUCTION

Multi-junction solar cells (MJSC) hold niche applications in the aero-space industry because of their high power conversion efficiency (PCE), light weight, and radiation resistance [1–3]. However, their high manufacturing cost has precluded them from use in terrestrial power generation. Recently, with the advent of epitaxy and the development of concentrators, the MJSCs have emerged as the most prominent technology for large-scale electricity generation, where the initial production cost can potentially be compensated by the high efficiency and minimal material usage [4]. Record efficiencies up to 43.5% have recently been reported from metamorphic and lattice matched triple junction solar cells under concentrated illumination [5,6]. In comparison, it would require roughly 100 times the material surface area to generate the same amount of power using silicon photovoltaic technology with an efficiency of 16% [7].

A basic MJSC device is modeled by series connected p–n diodes with material bandgaps engineered to absorb different portions of the solar spectrum. The wide absorption range can span wavelengths from 300 to 1800 nm for an InGaP/GaAs/Ge triple-junction solar cell (TJSC). However, the output current coming out of the device is ultimately limited by the smallest photocurrent generated by each sub-cell. Therefore, photon absorption must be taken into account to balance the current generation among sub-cells to maximize the PCE, commonly known as current matching. Conventional MJSCs utilize multiple dielectric thin film coatings with a graded refractive index (GRIN) profile for antireflection [8]. However, suppressing optical reflection in the UV regime is particularly challenging due to the lack of adequate dielectric materials with very low refractive indices, which in turn restricts the photogenerated current from the top cell [9]. In addition, issues related to material selection and thermal constant mismatch under concentrated illumination also hinder the performance of thin-film based antireflective coatings (ARCs). Over the past few years, bio-inspired nanostructures have demonstrated broadband antireflection characteristics because of sub-wavelength scale features that collectively function as a GRIN medium to photons [10–18]. The structures can be fabricated with a single-type material,

which guarantees both optical design robustness and mechanical durability. Moreover, refractive index engineering is also achievable via control of the side wall profiles, opening many possibilities for a variety of applications in optics and optoelectronics [19–22]. These characteristics are very desirable in MJSCs in order to fully exploit their wide absorption range and strict operation conditions. Yet, surface recombination and current matching issues arising from patterning still challenge the realization of biomimetic nanostructures on a few micrometer thick epitaxial layers for MJSCs. Herein, we demonstrate bio-inspired antireflective structures incorporated into a monolithically grown $In_{0.5}Ga_{0.5}P/In_{0.01}Ga_{0.99}As/Ge$ TJSC, which show a remarkable reduction of optical reflection in the UV regime. Such an improvement is hardly attainable with common thin-film coatings. Accordingly, the photocurrent and PCE achieve 11.6 mA/cm^2 and 25.3%, respectively under one-sun Air Mass 1.5, Globe (AM1.5G) illumination, which are superior to those of control devices because of an alleviated current-matching condition. Moreover, the nanostructured device also exhibits omnidirectional photocurrent enhancement, which is ideal for concentrator operation at large acceptance angles. Finally, a reflectance engineering approach, based on a rigorous coupled wave analysis (RCWA), is demonstrated to maximize the current output of a TJSC with biomimetic nanostructures, paving the way for their deployment in concentrator photovoltaics.

2. EXPERIMENTAL METHODS

The tandem solar cell used in this work was composed of an $In_{0.5}Ga_{0.5}P$ top-cell, an $In_{0.01}Ga_{0.99}As$ mid-cell, and a Ge bottom cell, which were connected by tunneling diodes and monolithically grown on a p-type Ge substrate (see Supporting Information for the full epitaxial structure). As illustrated in Figure 1, the process consists of five steps: (1) Definition of the GaAs ohmic layer using selective etching of ammonia between the cap GaAs and the $Al_{0.5}In_{0.5}P$ window layers for the frontal electrode. (2) Deposition of 1-μm-thick SiN_x using plasma-enhanced chemical vapor deposition (PECVD) for surface protection and the fabrication of sub-wavelength structures. The SiN_x layer has a refractive index of around 1.9 and a nearly-zero extinction coefficient, as characterized by an n&k analyzer (N&K Technology 1200, Sta. Clara, CA, USA). The layer was subsequently treated with oxygen plasma for a hydrophilic surface. (3) Spin-cast of polystyrene nanospheres on SiN_x as the sacrificial mask. A suspension mixture containing nanospheres in solution with water and ethanol at 1:1 wt% was applied to the substrate, followed by a two-step spin coating process (500 rpm 10 s, 2000 rpm 20 s). Nearly close-packed monolayer arrays with areas up to 5 cm in diameter were formed on the surface because of self-assembly. (4) Applying inductively-coupled reactive ion etching (ICP-RIE) to fabricate the nanostructures. The operating condition include an RF frequency and bias power of 13.56 MHz and 100 W, respectively, at 30 mTorr chamber pressure for 8.5 min under a gas mixture of CHF_3 and O_2 = 10:30 sccm through individual electronic mass flow controllers. A higher chamber pressure lowers the etch rate and results in rougher surfaces. However, the overall etch rate is mostly determined by the gas flow rate and bias power. The ratio of gas flow controls the lateral etching and hence influences the side wall profile considerably. Therefore, by collectively controlling these parameters, we can achieve the engineering of the sidewall profile. (5) Removal of the undesired nanostructures with an additional lithography step to expose the GaAs ohmic layer for the evaporation of metal contacts. The fabricated devices were then dissected into tiles with a 0.55 × 0.55 cm^2 surface area and a 5.6% metallic shadow ratio. The average device processing time is aprroximately 40 h using university facilities.

The reflectance spectra were performed with a UV/Visible/NIR spectrophotometer (Hitachi U4100, Hitachi Ltd., Tokyo, Japan) with a built-in integrating sphere at 10 irradiance incidence. The angle-resolved reflectance spectroscopic system utilized a custom-built 15-cm radius integrating sphere with a motor-controlled rotational sample stage and a spectrometer (SPM-002-ET, Photon-control Inc., Burnaby, BC, Canada) to obtain the reflective spectrum with respect to different incident angles. The

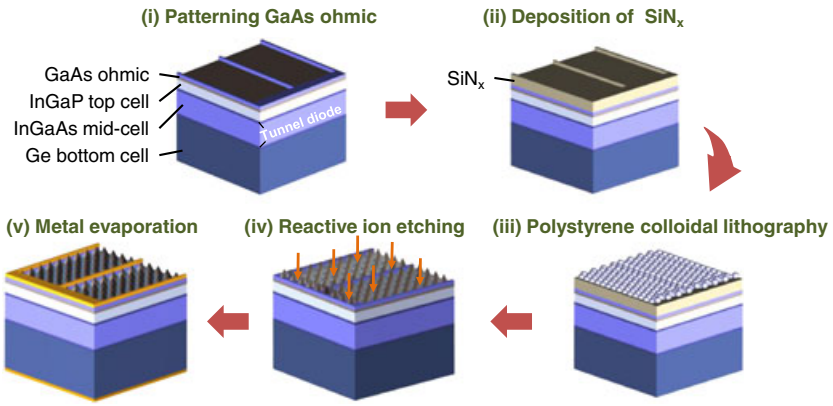

Figure 1. Schematic illustration of the fabrication of a multi-junction solar cell with SiN_x-based sub-wavelength structures.

system was calibrated by the reflective spectrum of a NIST-standard; intrinsic Si at normal incidence.

Due to the unavailability of an AM1.5D solar simulator and calibrated cell, the current-voltage properties were characterized under a simulated AM1.5G illumination at a standard test condition (25 °C, 1000 W/m^2). The spectrum of the solar simulator was measured by a calibrated spectroradiometer (Soma S-2440) in the wavelength range of 300–1100 nm. Before measurement, the intensity of the solar simulator was calibrated with a mono-crystalline silicon reference cell with a 2×2 cm^2 illumination area (VLSI Standards, Inc.). The omnidirectional property was examined by mounting cells on a customized rotatable chuck, and the photovoltaic performances were carried out under oblique AM1.5G conditions. The maximum measured angle is accurate up to 80°.

The external quantum efficiency (EQE) system employed a 300 W Xenon lamp (Newport 66984) light source and a monochromator (Newport 74112) with three gratings that cover the spectral range from 325 to 2700 nm. The beam spot at the sample was rectangular, measuring roughly 1×3 mm^2. An external light and voltage bias was used to select the junction for measurement. A calibration measurement was obtained at the beginning of each day using a calibrated silicon photodetector (Newport 818-UV) and a germanium photodetector (Newport 818-IR). The EQE measurement was performed using a lock-in amplifier (Standard Research System, SR830), an optical chopper unit (SR540) operated at 260 Hz chopping frequency, and a 1-ohm resistor in shunt connection to convert the photocurrent to voltage. The temperature of the cells during the measurements was actively controlled to be at 25 ± 1 °C.

3. RESULTS AND DISCUSSION

Figure 2(a) shows a photograph of polystyrene nanospheres self-assembled onto a 2-inch Ge wafer, where the grating-like color dispersion demonstrates the excellent periodicities present over the entire substrate. Figure 2(b) demonstrates the nearly close-pack monolayer assembly in large grains, which extends over a few micrometers. Despite the fact that the grain boundaries may seem defective in the formation of sub-wavelength structures at a large scale, the short range sixfold hexagonal symmetry actually mimics the arrangement of a moths' corneas, which adopt a random aperiodic domain structure without long range order [23,24]. The unique formation of domain arrays in moth eyes may deliberately contribute to their antireflective properties to a broad spectrum. The etching profile of sub-wavelength structures was controlled by tuning the ratio of gas flow, chamber pressure, and etching time cooperatively during RIE [25], as shown in the titled surface and cross-sectional scanning electron micrographs in Figure 2(c) and (d), respectively. Because the polystyrene nanospheres were also shrinking during the plasma etching, the fabricated sub-wavelength structures exhibit a smooth gradient side-wall profile, which resembles

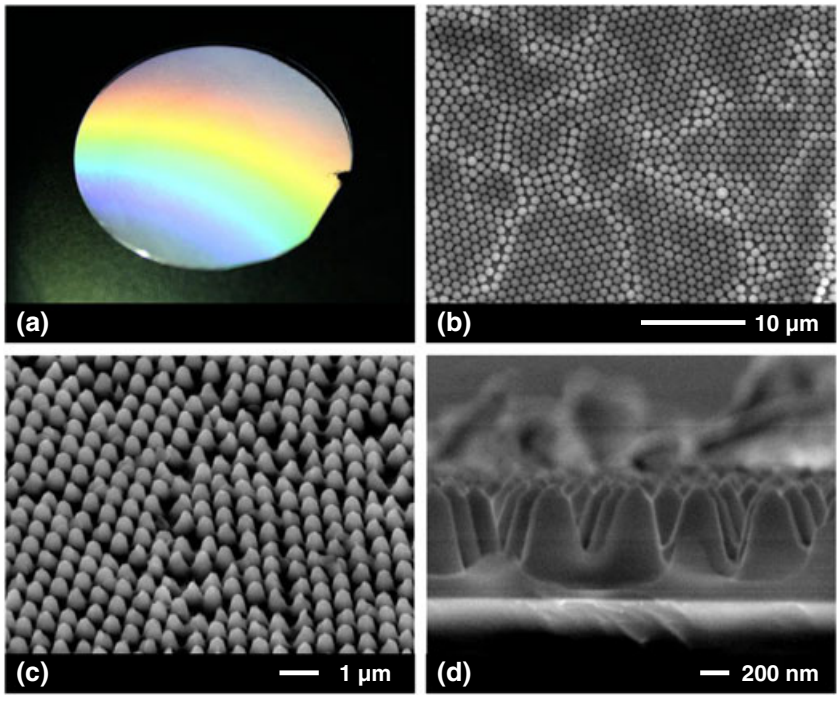

Figure 2. (a) Photograph of a two-inch Ge wafer with self-assembled polystyrene nanospheres showing uniform color dispersion. (b) Scanning electron micrographs of nearly close-packed monolayer arrangement of nanospheres with aperiodic domain structures, (c) tilted top view and (d) cross-sectional view of the fabricated sub-wavelength structures after reactive ion etching.

DOI: 10.1002/pip

moth-eye structures with a pitch of 600 nm and a depth of approximately 900 nm, determined by the nanosphere diameter and etching time, respectively. Finally, it can be seen in Figure 2(d) that approximately 100-nm-thick SiN_x was left un-etched to protect the exposed window layer surface of the top cell. The fabricated and control devices then underwent a series of optical and electric characterizations.

The optical reflectance spectra of the fabricated solar cells with bio-inspired sub-wavelength structures and with an 80-nm-thick SiN_x single-layer ARC were measured using an integrating sphere at 10° illumination incidence, and the results are plotted in Figure 3(a). It can be seen that the single-layer ARC exhibits very low-level reflection between the wavelengths of 500–700 nm due to destructive interference. On the other hand, the spectral response of the sub-wavelength structures is much flatter than the single-layer ARC. Overall, the net reduction of the absolute reflectance in UV can be as high as 35% at 310 nm wavelength, which is rarely achievable with available thin film coatings. The reflection suppression in the near-infrared also reaches around 10%, giving rise to an increased photocurrent from the middle and bottom sub-cells. Overall, the SiN_x-based sub-wavelength structures exhibit a superior AM1.5D-spectrum-weighted reflectance of 7.1% over the single-layer ARC of 9.4% in the 300–1700 nm wavelength range. We note that the level of optical reflection from the nanostructured surface is currently limited by the refractive index of SiN_x, where the GRIN profile can only be varied from $n = 1$ to $n = 1.9$. Hence, the antireflective properties could be further improved by fabricating sub-wavelength structures on a surface protection material with a refractive index close to that of the $In_{0.5}Ga_{0.5}P$ top cell ($n \sim 3.4$) to facilitate light transmission [26].

Next, we analyze the optical properties of the biomimetic nanostructures using angle-resolved reflectance spectroscopy. The measurements utilize an integrating sphere to capture both the specular and diffusive components of optical reflection from the surface of the control and nanostructured devices. As shown in Figure 3(b), the TJSC with a single-layer ARC suffers from a high reflection loss in the UV and near-infrared wavelength ranges, which further deteriorates for angles of incidence larger than 60°. In contrast, the reflectance map presented in Figure 3(c) displays the broadband and omni-directional antireflective properties from the nano-textured surface. To clarify the origins of the finite reflection loss, we have also measured the specular reflection of the same sample using an ellipsometer. The specular reflection in the measured wavelength range of 400–1000 nm is negligible. Therefore, we can conclude that the reflection loss is due to diffraction and scattering of light.

Before presenting the electric characterization results, Figure 4(a) shows the photographs of TJSCs with different antireflective treatments (from top to bottom): no ARC, single-layer ARC, and sub-wavelength structures. It can be seen that the nanostructured surface appears nearly black, compared with the purple color of a single-layer ARC surface.

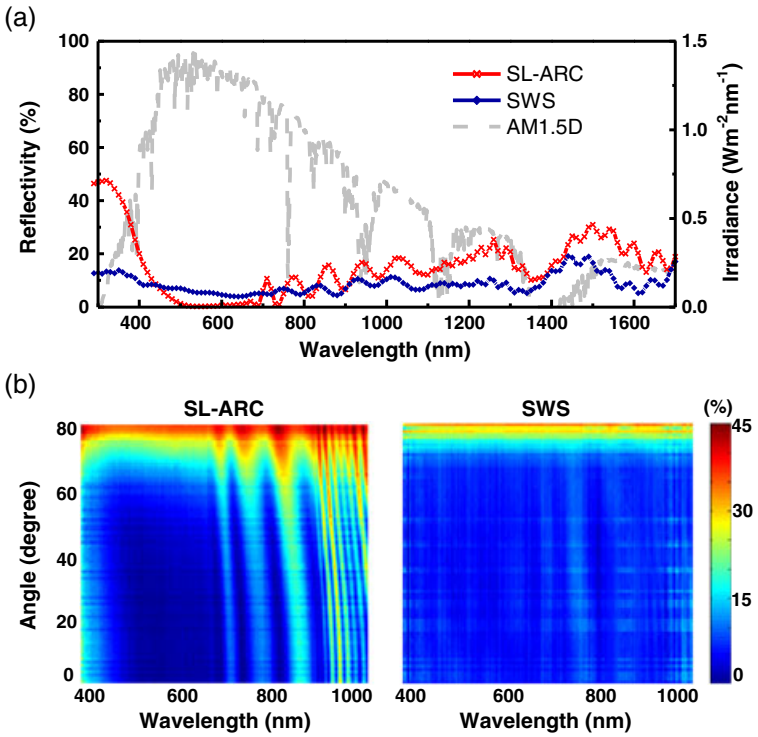

Figure 3. (a) The measured reflectance spectra at 10° irradiance incidence for triple junction solar cells with sub-wavelength structures (SWS) and with a single-layer antireflective coating (SL-ARC). An AM1.5D solar irradiance spectrum is plotted in dashed line for reference. (b) The angle-resolved reflectance spectra for both devices in the wavelength range of 400 nm to 1000 nm at an incident angle of 0° to 80°.

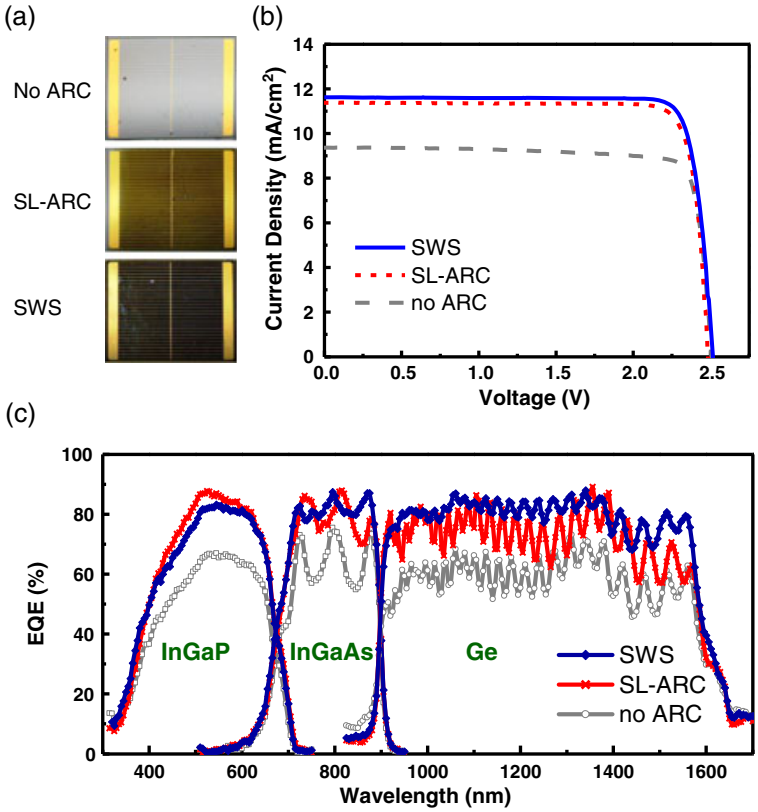

Figure 4. (a) Photographs of TJSCs with different antireflective treatments (from top to bottom): no antireflective coating (ARC), single-layer antireflective coating (SL-ARC), and sub-wavelength structures (SWS), respectively. The exposed nanostructured surface appears nearly black. (b) The current-voltage characteristics of TJSCs with different surface treatments under a simulated on-sun AM1.5G illumination condition. (c) The corresponding external quantum efficiency (EQE) of the $Ga_{0.5}In_{0.5}P$ top cell and $In0.01Ga_{0.99}As$ middle cell, and Ge bottom cell for the three devices: no-ARC in circle, SL-ARC in cross, and SWS in rhombus.

The measured current density–voltage (J–V) characteristics under a simulated AM1.5G illumination condition are plotted in Figure 4(b), where the three devices exhibit an open-circuit voltages (V_{oc}) of approximately 2.5 V. However, the short-circuit current density (J_{sc}) of the TJSC with sub-wavelength structures achieves 11.6 mA/cm^2, corresponding to an enhancement of 24.2% and 2.2% over the devices without an ARC and with a single-layer ARC, respectively. Overall, the PCE is considerably increased from 19.9% without any surface treatment to 25.3% with sub-wavelength structures, which is also superior to the 24.4% with single-layer ARC. The considerable improvement in J_{sc} and PCE over the bare device mainly arises from the suppressed surface reflection, instead of passivation due to SiN_x. This is because the surface recombination loss in MJSCs is primarily mitigated by the epitaxial window layer with a larger bandgap than that of the active layers to block the minority carriers. As a result, the enhancement could be further increased by choosing a sub-wavelength structure material with a higher refractive index than that of SiN_x. Moreover, the origins of the photocurrent enhancement are also investigated based on the EQE measurement of sub-cells for the three devices, as shown in Figure 4(c). The EQE spectrum is obtained by dividing the number of collected carriers to the number of incident photons at each wavelength. Therefore, the product of an EQE spectrum and the solar photon flux density integrated over wavelengths is proportional to the output photocurrent of a solar cell [27]. As seen in Figure 4(c), the Ge sub-cell exhibits the highest integrated photocurrent than the other two sub-cells for all three devices, which exclude it from being the current limit junction. Therefore, we only need to focus on the top two sub-cells and their antireflective design. First, for the reference device with a single-layer ARC, the integrated photocurrent from the InGaP top cell (14.2 mA/cm^2) is higher than that from the InGaAs middle cell (12.3 mA/cm^2), which results from an over-compensated antireflective design to increase the photocurrent output of the top cell. Such an approach is commonly seen in commercial devices to overcome the high surface reflection in the UV/blue wavelength range. On the other hand, the nanostructured surface successfully raises the output photocurrent for the middle cell (12.7 mA/cm^2) to better match with that of the top cell (13.6 mA/cm^2), leading to increased J_{sc} and PCE. In addition, although the Ge sub-cell is not the current-limit junction, the device with sub-wavelength structures still exhibits a large photocurrent enhancement over the control devices, offering an improved bottom-cell current for future tandem cells with different materials and large optical

absorption. For terrestrial applications of concentrator photovoltaics, the solar spectrum of interest is AM1.5D, instead of AM1.5G. Therefore, we can use the measured EQE spectra of sub-cells to calculate the output photocurrent under the AM1.5D spectrum. The respective photocurrent densities generated from the top and middle cells are 12.4 and 11.3 mA/cm2 for the device with a single-layer ARC, in contrast to 11.9 and 11.7 mA/cm2 for the device with sub-wavelength structures. Therefore, the limit photocurrent output increases from 11.3 to 11.7 mA/cm2, still representing a ~3.5% enhancement. Furthermore, the angular *J–V* characteristics were also measured to verify the impact of omni-directional antireflection. Figure 5 plots the normalized photocurrent density as a function of the incident angle, as well as the relative enhancement factor defined by Equation (1):

$$\text{Enhancement factor}(\theta) = \left(\frac{J_{\text{sc,SWS}}(\theta)}{J_{\text{sc,SLARC}}(\theta)} - 1\right) \times 100\%, \quad (1)$$

where $J_{\text{sc,SLARC}}(\theta)$ and $J_{\text{sc,SWS}}(\theta)$ respectively denote the measured photocurrent density for cells with a single-layer ARC and with sub-wavelength structures at oblique irradiance. We can see that the normalized angular photocurrent density with sub-wavelength structures nearly follows the referenced cosine curve up to 70° due to obliquely incident solar radiation. Such a characteristic indicates little dependence on the angular reflectance spectrum, $R(\lambda,\theta)$, as the angular photocurrent density $J_{\text{sc}}(\theta)$ can be expressed as Equation (2):

$$J_{\text{sc}}(\theta) = q\int IQE(\lambda)\cdot[1 - R(\lambda,\theta)]\cdot[BS(\lambda)\cdot\cos\theta]\mathrm{d}\lambda, \quad (2)$$

where $IQE(\lambda)$ represents the internal quantum efficiency; $BS(\lambda)\cos\theta$ represents the normal component of the photon flux density of an AM1.5G spectrum at an incident angle of θ and q is the electric charge. Therefore, besides the result shown in Figure 3(c), Figure 5 confirms that the omnidirectional antireflective properties of the nanostructured surface indeed increase the angular photocurrent. On the other hand, the angular photocurrent from the control device decays faster than the sub-wavelength structure, therefore limiting the PCE at large acceptance angles under concentrated illumination. With the characterizations of angular reflectance and photocurrent density, the presented sub-wavelength structures can certainly enhance the photocurrent output at very oblique irradiance incidence, which is vital for operation under a highly concentrated illumination condition. Meanwhile, as the cell temperature is also very high, the optical design for thin-film type ARCs may be shifted due to thickness variation induced by the thermal constant mismatch. On the other hand, the anti-reflection principle of sub-wavelength structures relies on the GRIN effect resulting from the structural profile, which has much less dependence on cell temperature. Looking forward, because the multi-junction solar cells have very thin and well balanced thicknesses, it is undesirable to fabricate nanostructures directly on the epilayers. Therefore, to further reduce the surface reflection presented in this work, it is essential to find a substitute material for SiNx with a refractive index closer to that of the top cell and with a lower optical loss (ideally zero) for the wavelengths of interest.

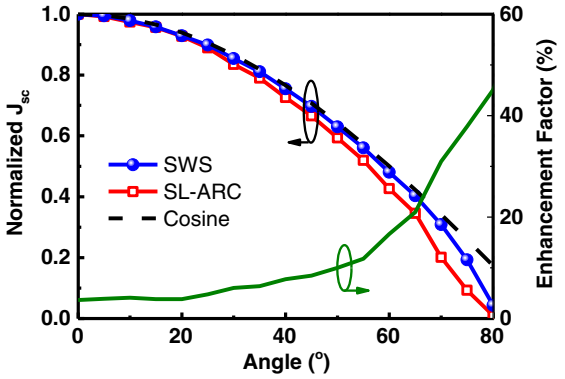

Figure 5. Normalized photocurrent densities for TJSCs with sub-wavelength structures (SWS) in circle and with a single-layer antireflective coating (SL-ARC) in square are characterized as a function of incident angles. The solid curve shows the corresponding enhancement factor at different incident angles. The dashed curve represents the cosine function for the oblique irradiance.

Finally, it is also of interest to understand how the structural parameters of sub-wavelength structures impact the output photocurrent of a TJSC. A practical design approach based on an RCWA method has been developed to first engineer the reflectance of sub-wavelength structures [25], and then match the current generated from sub-cells. The theoretical model is validated with the measured reflectance, which only shows a slight discrepancy for wavelengths below 450 nm due to material constant mismatch (see Supporting Information). Because the surface recombination loss is still quite high in UV, the mismatch has a negligible effect on the calculated photocurrent. Accordingly, the design scheme follows four simple steps:

(i) Calculate the reflectance spectrum, R(λ) as a function of the period and height of sub-wavelength structures using the RCWA method.
(ii) Obtain the internal quantum efficiency, $IQE(\lambda)$ of each sub-cell by dividing the measured $EQE(\lambda)$ with optical absorption, which equals to one minus the measured reflectance in the desired wavelength range.
(iii) Predict the photocurrent generated by the top and middle cells with sub-wavelength structures of different dimensions, denoted as $J_{\text{sc,top}}$ and $J_{\text{sc,mid}}$ respectively, using Equations (3) and (4):

$$J_{\text{sc,top}} = q\int_{320\text{nm}}^{750\text{nm}} IQE_{\text{top}}(\lambda)\cdot[1 - R(\lambda)]\cdot BS(\lambda)\ \mathrm{d}\lambda, \quad (3)$$

$$J_{\text{sc,mid}} = q\int_{550\,\text{nm}}^{950\,\text{nm}} IQE_{\text{mid}}(\lambda)\cdot[1 - R(\lambda)]\cdot BS(\lambda)\mathrm{d}\lambda, \quad (4)$$

(iv) Determine and plot the limited photocurrent using $J_{\text{sc}} = \min.[J_{\text{sc,top}}, J_{\text{sc,mid}}]$.

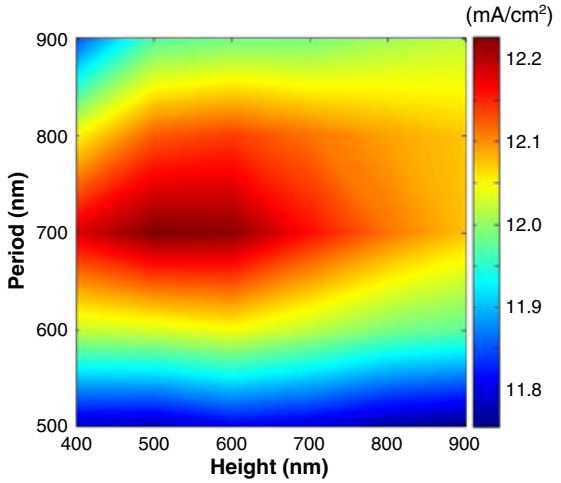

Figure 6. The calculated short circuit current densities of a TJSC for different periods and heights of SWS, taking into account the internal response of the top and middle sub-cells.

As shown in Figure 6, the J_{sc} is calculated for periodicities varying from 500 to 900 nm and heights from 400 to 900 nm. By taking into account the actual device response, the calculated photocurrent density (12.0 mA/cm^2) with a period and a height of 600 and 900 nm is very close to the measured (11.6 mA/cm^2) of the fabricated TJSC with sub-wavelength structures. According to the calculation, the optimized current density should ideally occur for sub-wavelength structures with a period of 700 nm and heights between 500 and 600 nm. It is worth noting that the parameters for sub-wavelength structures are highly correlated to the internal device response and the side wall profile, and hence need to be re-designed for solar cells made with different materials. Because the proposed optimization scheme is not tied to any specific devices/materials, the approach allows the design of sub-wavelength structures for general tandem cells.

4. CONCLUSION

In conclusion, we demonstrate the incorporation of bio-inspired nanostructures into a triple-junction solar cell, which overcomes the limited optical response of cells with a single-layer antireflective coating. The suppression of optical reflection in the UV and the omni-directional enhancement of photocurrent/efficiency characteristics are particularly remarkable compared with the control devices. By taking into account the internal device response of sub-cells, we also demonstrate a comprehensive design scheme to customize sub-wavelength structures that could fully exploit the wide-range absorption of multi-junction solar cells.

ACKNOWLEDGEMENTS

The authors thank Prof. Alex Freundlich at the ECE Department at the University of Houston, TX, USA for fruitful discussions. This project was founded by the National Science Council of Taiwan under grant number NSC96-2221-E-009-092-MY3 and NSC 98-2112-M-001-022-MY3.

REFERENCES

1. Yamaguchi M. Radiation-resistant solar cells for space use. *Solar Energy Materials and Solar Cells* 2001; **68**: 31.
2. Yamaguchi M, Okuda T, Taylor SJ, Takamoto T, Ikeda E, Kurita H. Superior radiation-resistant properties of InGaP/GaAs tandem solar cells. *Applied Physics Letters* 1997; **70**: 1566.
3. Green MA, Emery K, Hishikawa Y, Warta W. Solar cell efficiency tables (version 37). *Progress in Photovoltaics: Research and Applications* 2011; **19**: 84.
4. Guter W, Schöne J, Philipps SP, Steiner M, Siefer G, Wekkeli A, Welser E, Oliva E, Bett AW, Dimroth F. Current-matched triple-junction solar cell reaching 41.1% conversion efficiency under concentrated sunlight. *Applied Physics Letters* 2009; **94**: 223504.
5. King RR, Boca A, Hong W, Liu X-Q, Bhusari D, Larrabee D, Edmondson KM, Law DC, Fetzer CM, Mesropian S, Karam NH. Band-gap-engineered architectures for high-efficiency multijunction concentrator solar cells. *Proceedings of the the 24th European Photovoltaic Solar Energy Conference and Exhibition*, Hamburg, Germany, September 21–25, 2009; 55.
6. Solar Junction. Solar junction breaks concentrated solar world record with 43.5% efficiency [online]. Available: http://www.sj-solar.com/ [19 April 2011].
7. Luque A, Hegedus S. *Handbook of Photovoltaic Science and Engineering*. John Wiley and Sons: England, UK, 2003; 455.
8. Aiken DJ. High performance anti-reflection coatings for broadband multi-junction solar cells. *Solar Energy Materials and Solar Cells* 2000; **64**: 393.
9. Jung SM, Kim YH, Kim SI, Yoo SI. Design and fabrication of multi-layer antireflection coating for *III–V* solar cell. *Current Applied Physics* 2011; **11**: 538.
10. Clapham PB, Hutley MC. Reduction of lens reflexion by the "Moth Eye" principle. *Nature* 1973; **244**: 281.
11. Miller WH, Bernard GD, Allen JL. The optics of insect compound eyes. *Science* 1968; **162**: 760.
12. Wilson SJ, Hutley MC. The optical properties of 'moth eye' antireflection surfaces. *Journal of Modern Optics* 1982; **29**: 993.
13. Stork W, Streibl N, Haidner H, Kipfer P. Artificial distributed-index media fabricated by zero-order gratings. *Optics Letters* 1991; **16**: 1921.
14. Brundrett DL, Glytsis EN, Gaylord TK. Homogeneous layer models for high-spatial-frequency dielectric

surface-relief gratings: conical diffraction and antireflection designs. *Applied Optics* 1994; **33**: 2695.
15. Min W-L, Jiang B, Jiang P. Bioinspired self-cleaning antireflection coatings. *Advanced Materials* 2008; **20**: 3914.
16. Hobbs DS, MacLeod BD, Riccobono JR. Update on the development of high performance anti-reflecting surface relief micro-structures. *Proceedings of SPIE* 2007; **6545**: 65450Y.
17. Xi JQ, Schubert MF, Kim JK, Schubert EF, Chen MS, Lin Y, Liu W, Smart JA. Optical thin-film materials with low refractive index for broadband elimination of Fresnel reflection. *Nature Photonics* 2007; **1**: 176.
18. Yu P, Chang CH, Chiu CH, Yang CS, Yu JC, Kuo HC, Hsu SH, Chang YC. Efficiency enhancement of GaAs photovoltaics employing antireflective indium tin oxide nanocolumns. *Advanced Materials* 2009; **21**: 1618.
19. Wu HM, Lai CM, Peng LH. Optical response from lenslike semiconductor nipple arrays. *Applied Physics Letters* 2008; **93**: 211903.
20. Li Y, Zhang J, Yang B. Antireflective surfaces based on biomimetic nanopillared arrays. *Nano Today* 2010; **5**: 117.
21. Hsu C-M, Connor ST, Tang MX, Cui Y. Wafer-scale silicon nanopillars and nanocones by Langmuir–Blodgett assembly and etching. *Applied Physics Letters* 2008; **93**: 133109.
22. Choi K, Park SH, Song YM, Lee YT, Hwangbo CK, Yang H, Lee HS. Nanotailoring the surface structure for the monolithic high-performance antireflection polymer film. *Advanced Materials* 2010; **22**: 3713.
23. Stavenga DG, Foletti S, Palasantzas G, Arikawa K. Light on the moth-eye corneal nipple array of butterflies. *Proceedings of the Royal Society B* 2006; **273**: 661.
24. Srinivasarao M. Nano-optics in the biological world: beetles, butterflies, birds, and moths. *Chemical Reviews* 1999; **99**: 1935.
25. Chiu MY, Chang CH, Tsai MA, Chang FY, Yu P. Improved optical transmission and current matching of a triple-junction solar cell utilizing sub-wavelength structures. *Optics Express* 2010; **18**: A308.
26. Wrobel AM, Wickramanayaka S, Nakanishi Y, Fukuda Y, Hatanaka Y. Remote hydrogen plasma chemical vapor deposition of amorphous hydrogenated silicon-carbon films from an organosilane molecular cluster as a novel single-source precursor: structure, growth mechanism, and properties of the deposit. *Chemistry of Materials* 1995; **7**: 1403.
27. Nelson J. *The Physics of Solar Cells*. Imperial College Press: England, UK, 2003; 7.